Evaluation of a Heuristic Model for Tropical Cyclone Resilience

Paul D. Reasor[1] and Michael T. Montgomery[2]

[1]NOAA/AOML/Hurricane Research Division, Miami, Florida

[2]Department of Meteorology, Naval Postgraduate School, Monterey, California

Submitted to *Journal of the Atmospheric Sciences*

October 24, 2014

Revised January 26, 2015

Corresponding author address: Paul D. Reasor, Hurricane Research Division, NOAA/AOML, Miami, FL 33149.
E-mail: paul.reasor@noaa.gov

Report Documentation Page

Form Approved
OMB No. 0704-0188

Public reporting burden for the collection of information is estimated to average 1 hour per response, including the time for reviewing instructions, searching existing data sources, gathering and maintaining the data needed, and completing and reviewing the collection of information. Send comments regarding this burden estimate or any other aspect of this collection of information, including suggestions for reducing this burden, to Washington Headquarters Services, Directorate for Information Operations and Reports, 1215 Jefferson Davis Highway, Suite 1204, Arlington VA 22202-4302. Respondents should be aware that notwithstanding any other provision of law, no person shall be subject to a penalty for failing to comply with a collection of information if it does not display a currently valid OMB control number.

1. REPORT DATE **26 JAN 2015**	2. REPORT TYPE	3. DATES COVERED **00-00-2015 to 00-00-2015**
4. TITLE AND SUBTITLE **Evaluation of a Heuristic Model for Tropical Cyclone Resilience**		5a. CONTRACT NUMBER
		5b. GRANT NUMBER
		5c. PROGRAM ELEMENT NUMBER
6. AUTHOR(S)		5d. PROJECT NUMBER
		5e. TASK NUMBER
		5f. WORK UNIT NUMBER
7. PERFORMING ORGANIZATION NAME(S) AND ADDRESS(ES) **Naval Postgraduate School,Department of Meteorology,Monterey,CA,93943**		8. PERFORMING ORGANIZATION REPORT NUMBER
9. SPONSORING/MONITORING AGENCY NAME(S) AND ADDRESS(ES)		10. SPONSOR/MONITOR'S ACRONYM(S)
		11. SPONSOR/MONITOR'S REPORT NUMBER(S)

12. DISTRIBUTION/AVAILABILITY STATEMENT
Approved for public release; distribution unlimited

13. SUPPLEMENTARY NOTES

14. ABSTRACT

This work examines the applicability of a previously-postulated heuristic model for the 4 temporal evolution of the small-amplitude tilt of a tropical cyclone-like vortex under 5 vertical-shear forcing for both a dry and cloudy atmosphere. The heuristic model hinges 6 on the existence of a quasi-discrete vortex-Rossby wave and its ability to represent the 7 coherent precession and tilt-decay of a stable vortex in the free-alignment problem. 8 Linearized numerical solutions for a dry and cloudy vortex confirm the model predictions 9 that an increase in the magnitude of the radial potential vorticity (PV) gradient within the 10 vortex skirt surrounding the core yields a more rapid evolution of a sheared vortex 11 towards the equilibrium, left-of-shear tilt configuration. However, in the moist-neutral 12 limit, in which the effective static stability vanishes in rising and sinking regions, the 13 heuristic model yields a poor approximation to the simulated vortex core evolution, but a 14 left-of-shear tilt of the near-core vortex, radially beyond the heating region, remains the 15 preferred long-time solution. Within the near-core skirt the PV perturbation generated by 16 vertical shearing exhibits continuous-spectrum type vortex-Rossby waves, features that 17 are not captured by the heuristic model. Nevertheless, the heuristic model continues to 18 predict the rapid vertical alignment and equilibrium, left-of-shear tilt configuration of the 19 simulated near-core vortex in the moist-neutral limit.

15. SUBJECT TERMS

16. SECURITY CLASSIFICATION OF:			17. LIMITATION OF ABSTRACT	18. NUMBER OF PAGES	19a. NAME OF RESPONSIBLE PERSON
a. REPORT **unclassified**	b. ABSTRACT **unclassified**	c. THIS PAGE **unclassified**	**Same as Report (SAR)**	**51**	

ABSTRACT

This work examines the applicability of a previously-postulated heuristic model for the temporal evolution of the small-amplitude tilt of a tropical cyclone-like vortex under vertical-shear forcing for both a dry and cloudy atmosphere. The heuristic model hinges on the existence of a quasi-discrete vortex-Rossby wave and its ability to represent the coherent precession and tilt-decay of a stable vortex in the free-alignment problem. Linearized numerical solutions for a dry and cloudy vortex confirm the model predictions that an increase in the magnitude of the radial potential vorticity (PV) gradient within the vortex skirt surrounding the core yields a more rapid evolution of a sheared vortex towards the equilibrium, left-of-shear tilt configuration. However, in the moist-neutral limit, in which the effective static stability vanishes in rising and sinking regions, the heuristic model yields a poor approximation to the simulated vortex core evolution, but a left-of-shear tilt of the near-core vortex, radially beyond the heating region, remains the preferred long-time solution. Within the near-core skirt the PV perturbation generated by vertical shearing exhibits continuous-spectrum type vortex-Rossby waves, features that are not captured by the heuristic model. Nevertheless, the heuristic model continues to predict the rapid vertical alignment and equilibrium, left-of-shear tilt configuration of the simulated near-core vortex in the moist-neutral limit.

1. Introduction

The impact of environmental vertical wind shear on tropical cyclone (TC) structure and intensity depends on the TC's dynamic resilience (Jones 1995; Reasor et al. 2004) and interaction with environmental dry air (Simpson and Riehl 1958; Kimball 2006; Riemer and Montgomery 2011), both of which influence the organization of convection and, ultimately, operation of the TC power machine (Emanuel et al. 2004; Riemer et al. 2010, 2013; Tang and Emanuel 2010, 2012).

The problem of dynamic resilience focuses on the ability of the TC to maintain a vertically-coherent vortex structure as it experiences vertical shearing. Jones (1995) found that the coupling between vertical layers, and tendency for the upper- and lower-level potential vorticity (PV) of the cyclonic core to precess into an upshear-tilted configuration, restricts the development of vertical tilt that would otherwise occur through differential advection. For small-amplitude displacements between the upper- and lower-level circulations, Reasor et al. (2004; hereafter RMG04) developed a heuristic model for the vertical shear forcing of vortex tilt, demonstrating that the tilt evolution depends not only on the intrinsic rotation and scales of the flow (e.g., Rossby number and Rossby deformation radius), but also on the radial distribution of PV in the core region of the vortex. Here, we further evaluate this heuristic model.

While RMG04 showed that dramatically different vortex evolution could be expected for different vortex profiles, they did not consider a set of controlled experiments to isolate the specific impact of the near-core profile on the sheared vortex evolution. To understand why such dependence might exist in the first place, consider the idealized vortex depicted in Fig. 1. The vortex core is defined as the innermost region of

the vortex bounded approximately by the radius of maximum PV gradient, r_c. The vortex skirt immediately surrounds the core and is characterized by PV values much less than found within the core. We will alternately refer to this portion of the vortex as the near-core region, and the sum of the core and skirt as the core region.

When a vortex is tilted, as would be accomplished by a burst of vertical shear flow from the environment, the PV of the core will be deformed. In the limit of small but finite-amplitude tilt, the dynamics of the core can be meaningfully described by the evolution of a vortex-Rossby wave (VRW) asymmetry, referred to as a tilt quasimode, on a background axisymmetric flow (Reasor and Montgomery 2001). Schecter et al. (2002) alternatively described the VRW tilt asymmetry as a discrete mode. In this latter interpretation, a resonance may occur at the critical radius r_* where the precession frequency of the tilt mode equals the angular rotation rate of the background flow. As explained in Schecter et al. (2002) through canonical angular momentum (and equivalently, angular wave activity) conservation arguments, stirring of the flow near the critical radius requires a damping of the tilt mode if the radial gradient of PV at r_* is negative. Since the growth in PV perturbation amplitude at r_* depends intrinsically on how sloped the background PV profile is there, the rate at which this damping occurs, hence the vortex resilience, will be proportional to the magnitude of the PV gradient within the vortex skirt. RMG04 extended these ideas to the shear-forced problem. In section 3 we revisit their heuristic model for the vortex evolution in shear, which predicts a similar dependence of resilience on the PV gradient at r_*.

Since moist convection pervades tropical cyclones, especially in their core region, it is still unclear whether the resonant damping mechanism using dry dynamics governs

to leading order the vortex resilience in shear. For one thing, the static stability is locally reduced within moist convective regions of the flow (e.g., Durran and Klemp 1982; Emanuel et al. 1987). RMG04 observed that a uniform reduction of the static stability throughout the flow can lead to a change in the resilience mechanism from one governed by resonant damping to one that shows greater consistency with the classic axisymmetrization process and spiral wind up (e.g., Melander et al. 1987; Smith and Montgomery 1995; Montgomery and Kallenbach 1997). They did not, however, explicitly consider the impacts of *local* static stability reduction on the resilience mechanism. To the extent that the resonant damping mechanism may still govern the resilience of a moist-convective vortex, RMG04 reasoned that the impact of heating would be to reduce the local deformation radius, thereby increasing the azimuthal propagation speed of the tilt mode. An increased propagation speed would, in turn, shift r_* inward toward the core where the PV gradient is larger, leading to more effective damping of the tilt mode (e.g., Schecter and Montgomery 2007; see their Figs. 10 and 11 and accompanying discussion). In a recent moist numerical study of TCs in shear, Riemer et al. (2013) documented differences in vortex tilt evolution potentially related to differences in the initial radial vorticity profile outside the core. To investigate this important issue, we will consider the sheared vortex evolution under a simple parameterization of convective heating for a cloudy vortex. Here “cloudy” refers to regions of non-precipitating, saturated air. The results with neutral stratification within a limited “eyewall” region will show that the heuristic model poorly approximates the overall simulated vortex evolution, calling for further treatment of the moist problem to fully understand the mechanisms for TC resilience.

The paper is organized as follows. Section 2 presents the numerical model with shear forcing and parameterized convective heating. The heuristic model for the shear-forced evolution of vortex tilt is reviewed in section 3. Idealized numerical simulations, which address the relevance of the near-core profile, are presented here. Section 4 then considers the shear-forced evolution of a cloudy vortex. A discussion of our results and conclusions are presented in section 5.

2. Model

Our numerical simulations of the idealized TC in shear will use the linear primitive equation model described in RMG04, modified here to include a parameterization of diabatic heating. The model assumes a stably stratified fluid and employs the Boussinesq approximation on an f plane. The model is formulated in a cylindrical coordinate system (r, φ, z), where r is radius, φ is azimuthal angle, and z is the pseudoheight vertical coordinate (Hoskins and Bretherton 1972), and is bounded vertically by isothermal rigid lids at $z = 0$ and $z = H$. Consistent with small but finite amplitude departures from vertical alignment, the governing equations are linearized about a circular (mean) vortex in gradient and hydrostatic balance. The mean vortex and quasi-static flow perturbation (i.e., the tilt asymmetry) are then decomposed into barotropic and internal baroclinic modes. As in RMG04, for simplicity, we consider only initially barotropic mean vortices. Under the Boussinesq approximation, the vertical structure of the modes comprising the geopotential is then given by $\cos(m\pi z/H)$, where m is the vertical mode number and H is the physical depth of the vortex, taken to be 10 km in all experiments.

The tilt asymmetry is Fourier decomposed in azimuth. The prognostic primitive equations for each vertical (m) and azimuthal (n) mode subject to vertical shear forcing are given as follows:

$$\left(\frac{\partial}{\partial t}+in\overline{\Omega}\right)\hat{u}_{mn}(r,t)-\overline{\xi}\hat{v}_{mn}+\frac{\partial\hat{\phi}_{mn}}{\partial r}=-\alpha(r)\hat{u}_{mn}+F_{u,s}\,, \tag{1}$$

$$\left(\frac{\partial}{\partial t}+in\overline{\Omega}\right)\hat{v}_{mn}(r,t)+\overline{\eta}\hat{u}_{mn}+\frac{in}{r}\hat{\phi}_{mn}=-\alpha(r)\hat{v}_{mn}+F_{v,s}\,, \tag{2}$$

$$\left(\frac{\partial}{\partial t}+in\overline{\Omega}\right)\hat{\phi}_{mn}(r,t)+Y(r)\,c_m^2\left[\frac{1}{r}\frac{\partial}{\partial r}(r\hat{u}_{mn})+\frac{in\hat{v}_{mn}}{r}\right]=-\alpha(r)\hat{\phi}_{mn}+F_{\phi,s}\,, \tag{3}$$

where $\hat{u}_{mn}$, $\hat{v}_{mn}$, and $\hat{\phi}_{mn}$ are the radial velocity, tangential velocity, and geopotential Fourier amplitudes, respectively. The basic state vortex quantities, $\overline{\Omega}=\overline{v}/r$, $\overline{\xi}=f+2\overline{\Omega}$, and $\overline{\eta}=f+\overline{\zeta}$, are the azimuthal-mean angular velocity, modified Coriolis parameter, and absolute vertical vorticity, respectively. Here $\overline{\zeta}=r^{-1}\,d(r\overline{v})/dr$ is the relative vertical vorticity and f is the constant Coriolis parameter, taken to be 3.53×10^{-5} s^{-1} (corresponding to 14º latitude) in all experiments. The internal gravity wave phase speed $c_m=NH/m\pi$, where N is the Brunt-Väisälä frequency and is assumed to take a constant value of 1.22×10^{-2} s^{-1} in all cases. The internal gravity wave phase speed for m = 1 is approximately 40 m s^{-1}. The function $Y(r)$ is a buoyancy reduction factor (Schecter and Montgomery 2007) accounting for radial variations in the static stability in the core region, and is further motivated below. The first term on the rhs of each equation represents Rayleigh damping within a "sponge" ring at the outermost portion of the computational domain so as to prevent the spurious reflection at the outer boundary of outward-propagating inertia-gravity waves generated from the vortex-shear interaction in

the core region. The sponge ring extends inward 150 km from the outer boundary with a peak damping rate of 1/300 s^{-1}. A 3000-km outer radius domain with radial grid spacing Δr = 1 km is used in the experiments of section 3. In the cloudy vortex experiments of section 4, the domain extends to 1600 km with a finer grid spacing of Δr = 0.5 km. Additional details of the numerical system can be found in RMG04.

The mean PV for a barotropic vortex, $\overline{q} = N^2\overline{\eta}$, is prescribed and the associated tangential velocity field is assumed in gradient balance:

$$f\overline{v} + \frac{\overline{v}^2}{r} = \frac{d\overline{\phi}}{dr}. \tag{4}$$

The PV perturbation amplitude derived from Eqs. (1)-(3) is given by

$$\hat{q}_{mn} = N^2\hat{\zeta}_{mn} - \left(\frac{m\pi}{H}\right)^2 \overline{\eta}\hat{\phi}_{mn}. \tag{5}$$

In the linear framework here, a tilted vortex is approximated by adding to $\overline{q}$ a PV perturbation with $m = n = 1$ and radial structure proportional to the radial gradient of $\overline{q}$. This approximation to a tilt asymmetry takes the form of a wavenumber-1 dipole with reflection about $z = H/2$. Details of the method for obtaining quasi-balanced perturbation asymmetric wind and geopotential fields are described in RMG04.

The second term on the rhs of Eqs. (1)-(3) is a linearized forcing term that arises with the presence of an imposed zonal vertical shear flow, which is assumed weak compared to the basic state swirling flow. For simplicity, the zonal shear flow is chosen to have vertical structure of the first internal baroclinic mode so that only vortex perturbations with $m = n = 1$ are forced. In cylindrical coordinates, the radial and azimuthal velocity components of the shear flow forcing are expressed as

$$u_s = U\cos(\varphi)\cos\left(\frac{\pi z}{H}\right),$$

$$v_s = -U\sin(\varphi)\cos\left(\frac{\pi z}{H}\right), \tag{6}$$

where U is the zonal velocity at z = 0. After neglecting products of shear and vortex perturbation terms in the resulting primitive equations, the linearized shear forcing terms in Eqs. (1)-(3) are then as follows:

$$F_{u,s} = \frac{1}{2} iU\overline{\Omega}, \qquad F_{v,s} = -\frac{1}{2} U\frac{d\overline{v}}{dr}, \qquad F_{\phi,s} = \frac{1}{2} fU\overline{v}. \tag{7}$$

To represent the convective heating/cooling processes, we follow the thermodynamically reversible formulation of Schecter and Montgomery (2007) and introduce the heating into the equivalent mass-continuity Eq. (3). Under the assumption of hydrostatic motions, they derived a thermodynamic equation in pressure coordinates which contains expressions for the moist adiabatic derivative of density potential temperature with respect to pressure, holding moist entropy and total water mixing ratio constant, in saturated and unsaturated air. The wave equations for a TC-like vortex containing both clear (i.e., unsaturated) and cloudy (i.e., saturated) regions were derived by neglecting the product of the vertical motion asymmetries with asymmetries in the thermodynamic derivatives. Although mathematically consistent, the accuracy of such an approximation in the context of the tilt asymmetry evolution has not yet been explored systematically. In the resulting thermodynamic equation, the term involving the static stability is modified from its dry counterpart through the addition of a buoyancy reduction factor $Y(r, p)$, which accounts for the azimuthally-averaged clear and cloudy air stability properties (Schecter and Montgomery 2007). In essence, the presence of cloudy

air leads to a reduction of the azimuthal-mean static stability (cf. Patra 2004). For the barotropic mean vortices considered here, we assume Y is independent of height. Thus, the thermodynamic equation of RMG04 is modified by replacing the constant N^2 with $Y(r)N^2$ in Eq. (3). In the case of a clear (non-cloudy) vortex, $Y \rightarrow 1$ and the dry thermodynamic equation of RMG04 is recovered. In the eyewall of a hurricane, we can anticipate values of Y approaching zero (Schecter and Montgomery 2007; see their Fig. 2).

For the cases examined here (Table 1), simulation experiments are performed with and without vertical wind shear. In the absence of shear, the vortex is given an initial tilt as described above. The ensuing vortex evolution is referred to here as 'free alignment.' In the experiments of section 3, a dry Rankine-with-skirt (RWS) vortex is used. The vortex radial profiles shown in Fig. 2a are similar except for different radial gradients of PV within the skirt immediately outside the core. The vortex of the control experiment RWS1 exhibits the weakest gradient within the skirt. Compared to RWS1, the vortices of RWS2 and RWS3 have radial PV gradients that are 33% and 100% greater, respectively. The RWS2 and RWS3 vortices do have greater circulation outside the core, but in all cases the contribution of the skirt to the total circulation in the core region is small. Inside r = 69 km (the critical radius estimated below in section 3b) of the RWS1, RWS2, and RWS3 vortices, the skirt contributes approximately 3.8%, 4.4%, and 5.7%, respectively, to the total circulation.

The vortex radial profile shown in Fig. 2b is used in the "cloudy vortex" experiments of section 4. It is based upon low-level radar and fight-level observations of Hurricane Guillermo (1997; Reasor and Eastin 2012). A monotonic approximation to the

observed PV profile is used here to exclude the possibility of 'dry' exponential barotropic instability (Schubert et al. 1999) and the trochoidal wobble-mode instability (Nolan et al. 2001)[1]. In a series of experiments, discussed further in section 4, the static stability within the region of strongest winds is varied from the limit of no heating (OBS1) to the limit of neutral values (OBS5).

3. Dependence of Vortex Evolution on Near-core PV Profile

a. A heuristic model revisited

For vertically sheared vortices like those described in section 2, the phase and amplitude evolution of the tilt asymmetry may be understood through a simple heuristic model. As in RMG04, we assume that the vortex admits a free-alignment solution in which the tilt asymmetry takes the form of a damped discrete VRW mode (Schecter and Montgomery 2003). The PV perturbation may then be expressed (for $m = n = 1$) as

$$q'(r,\varphi,z,t) = A(r)e^{\gamma_{cl}t}e^{i(\varphi-\omega_p t)}\cos\left(\frac{\pi z}{H}\right) + c.c., \qquad \gamma_{cl} < 0, \tag{8}$$

where the complex amplitude $A(r)$ provides the radial structure of the tilt asymmetry, γ_{cl} is the exponential (Landau) damping rate (Briggs et al. 1970), ω_p is the vortex precession frequency and "*c.c.*" denotes complex conjugate. Here γ_{cl} is defined as negative for the decaying mode. The temporal part of (8) is the solution to a single-component damped harmonic oscillator equation of the form

$$\frac{dq'}{dt} + \left(i\omega_p - \gamma_{cl}\right)q' = 0\,. \tag{9}$$

[1] Exponential growth of perturbations may still occur through the excitation of inertia-gravity waves by the rotating tilt asymmetry (Schecter and Montgomery 2004, 2006).

Equation (9) may be motivated physically from a re-casting of the linearized PV equation without shear forcing:

$$\left(\frac{\partial}{\partial t}+\overline{\Omega}\frac{\partial}{\partial \varphi}\right)q'(r,\varphi,z,t)+u'\frac{d\overline{q}}{dr}=0\,. \tag{10}$$

Note that Eq. (10) does not explicitly contain the PV source term derived from the diabatic heating in the system (1)-(3). In the heuristic model given by Eq. (9) the response to heating is represented through a modification of the mode's propagation. The PV equation (10) is consistent with this approximation. The heuristic model for the shear-forced system is derived by first introducing to the rhs of Eq. (10) the linearized shear forcing consistent with (7),

$$F_s' = -U\left\{\frac{d\overline{q}}{dr}+\frac{\overline{v}}{\ell_{r,G}^2}\frac{\overline{q}}{f}\right\}\cos(\varphi)\cos\left(\frac{\pi z}{H}\right), \quad m = 1. \tag{11}$$

Here $\ell_{r,G} = NH/\pi f$ is the "global" Rossby deformation radius of the flow (for m = 1). The forced, damped core-mode model derived below is partly justified by the strong projection of the above shear forcing onto the tilt mode wavefunction (cf. Schecter et al. 2000). The solution to Eq. (9) with the forcing (11) added to the rhs is

$$q'(r,\varphi,z,t)=A(r)e^{\gamma_{cl}t}e^{i(\varphi-\omega_p t)}\cos\left(\frac{\pi z}{H}\right)-\frac{U}{i\omega_p-\gamma_{cl}}\left\{\frac{d\overline{q}}{dr}+\frac{\overline{v}}{\ell_{r,G}^2}\frac{\overline{q}}{f}\right\}\frac{e^{i\varphi}}{2}\cos\left(\frac{\pi z}{H}\right)+c.c. \tag{12}$$

The second term in the shear forcing (11), and which appears in the solution (12), is associated with the horizontal advection of vertical shear-flow PV by the basic state vortex flow. Within the core region of the vortices in Fig. 2, a scale analysis and calculation show that this term is at least an order of magnitude smaller than the first term representing the differential advection of basic state vortex PV by the vertical shear flow.

Thus, for the vortices here, the solution may be further simplified by neglecting this second term of the shear forcing:

$$q'(r,\varphi,z,t) \approx A(r)\, e^{\gamma_{cl} t} e^{i(\varphi-\omega_p t)} \cos\left(\frac{\pi z}{H}\right) - \frac{U}{i\omega_p - \gamma_{cl}} \frac{d\overline{q}}{dr} \frac{e^{i\varphi}}{2} \cos\left(\frac{\pi z}{H}\right) + c.c. \qquad (13)$$

Note an implicit assumption in the derivation of (12) and (13) is that γ_{cl} and ω_p of the free-alignment solution (8) continue to govern the forced evolution of the vortex. In the fully nonlinear problem this should be a valid approximation provided the shear forcing is relatively weak.

Assuming the initial vortex is vertically aligned and $\left|\gamma_{cl}/\omega_p\right| << 1$ (Schecter and Montgomery 2003), it follows analytically from (13) that in the large-time limit the forced solution will be governed approximately by

$$q'(r,\varphi,z,t) \approx \frac{U}{\omega_p} \frac{d\overline{q}}{dr} \left[e^{\gamma_{cl} t} \sin(\varphi - \omega_p t) - \sin\varphi \right] \cos\left(\frac{\pi z}{H}\right). \qquad (14)$$

This heuristic model predicts that small but finite damping results in a long-time solution of fixed tilt as measured by the amplitude and phase of the PV asymmetry. Since $d\overline{q}/dr$ is negative outside the core for "real-world" TC vortices (Mallen et al. 2005), the equilibrium vortex tilt is directed 90º left of shear. Furthermore, since γ_{cl} is proportional to the PV gradient at the critical radius r_* of the discrete VRW (from the free-alignment solution), the resilience of the shear-forced vortex should depend upon the near-core tangential wind profile. We validate this prediction of the heuristic model through explicit numerical simulations discussed below. The heuristic model solution (14) in the limit of $\gamma_{cl} = 0$ has recently been confirmed by Päschke et al. (2012) for the fully

nonlinear problem through the method of matched asymptotic expansions. Note that in this limit (14) may be re-expressed as

$$q'(r,\varphi,z,t) \approx -\frac{2U}{\omega_p}\frac{d\overline{q}}{dr}\sin\left(\frac{\omega_p t}{2}\right)\cos\left(\varphi-\frac{\omega_p t}{2}\right)\cos\left(\frac{\pi z}{H}\right). \tag{15}$$

Thus, according to the heuristic model in the absence of damping, the shear-forced tilt asymmetry should precess with half the frequency of the intrinsic tilt mode in the free-alignment case.

b. Heuristic model validation

As noted in section 2, the RWS vortices used in RWS1-3 differ primarily in the gradient of PV within the near-core skirt (Fig. 2a). The intrinsic resilience of each vortex is explored first by adding to the symmetric vortex the balanced PV perturbation approximating the $m = n = 1$ tilt asymmetry. For brevity, we will denote the geopotential Fourier amplitude for $m = n = 1$ by $|\phi_1|$ and the corresponding three-dimensional perturbation value by ϕ_1. A similar convention will be employed for all perturbation variables. A time series of the geopotential perturbation amplitude evaluated at the core radius r_c is shown in Fig. 3. Here and elsewhere, time is expressed in units of circulation period, defined here as $2\pi/\overline{\Omega}(r_c)$.

From Fig. 3, during the first circulation period, the asymmetry adjusts as it takes the form of the tilt mode. Thereafter, the decay of the tilt asymmetry is approximately exponential[2] for multiple circulation periods, consistent with prior theoretical analyses (Schecter et al. 2002; Schecter and Montgomery 2003). While semi-analytical methods

[2] The low-frequency oscillations in amplitude result from the initialization of PV perturbation in the critical layer of the tilt mode (Schecter and Montgomery 2006). The oscillations are thus not a fundamental feature of the solution.

exist to compute ω_p and γ_{cl} (e.g., Schecter et al. 2002, Appendix), we estimate the values here by constructing linear best fits to the simulated geopotential phase and (logarithmically-scaled) amplitude following the initial adjustment period. It is important to recognize, however, that the numerical solution reflects both the effects of resonant damping and tilt asymmetry growth through inertia-gravity wave (IGW) pumping (Schecter and Montgomery 2004, 2006). Thus, the decay rate estimated here is actually the sum of the (negative) resonant damping rate γ_{cl} and (positive) exponential IGW pumping rate γ_{rad}. We define $\gamma = \gamma_{rad} + \gamma_{cl}$ as the net decay rate to avoid confusion.

Table 2 lists the estimated values of r_*, ω_p, and γ for each of the three RWS experiments. The value of ω_p increases slightly from RWS1 to RWS3 due to the increased amount of circulation immediately outside the core. This increase has negligible impact on the value of r_*. The value of γ, however, increases by an order of magnitude with the doubling of the PV gradient within the skirt. Schecter and Montgomery (2003) showed that the resonant damping rate γ_{cl} is directly proportional to the PV gradient at r_*. In the absence of IGW pumping, then, the decay rate ought to approximately double from RWS1 to RWS3. Note that if the IGW pumping were to largely offset the resonant damping in RWS1, but not in RWS3, then γ could in principle increase by a factor substantially larger than 2. The weak decay observed in Fig. 3 for RWS1 suggests that this is a plausible explanation for the order-of-magnitude increase in net decay rate[3].

[3] Estimates of γ_{rad} and γ_{cl} using the simulated solution amplitudes in the analytical expressions of Schecter and Montgomery (2004, Eqs. 61 and 68) suggest that γ_{cl} is only ~7.5% larger than γ_{rad} in

The same vortices with no initial vertical tilt are then subjected to unidirectional shear. In all cases we take U = -2 m s^{-1}, yielding 4 m s^{-1} of deep-layer westerly shear. Figure 4 shows the PV perturbation amplitude measured at r_c and the direction of tilt, defined here as the PV perturbation crest azimuth at $z = H$, for each case[4]. In RWS1 the vortex tilts, precesses upshear, and realigns on a time scale of 5 circulation periods. This evolution is then repeated. The direction and amplitude show signs of a slow approach to a quasi-equilibrium state. The rotation frequency estimated from the PV asymmetry phase in Fig. 4a is approximately half the value of ω_p for this weakly-damped case, in agreement with the heuristic model prediction given by (15). The increased skirt PV gradient in RWS2 and RWS3 does in fact lead to a more rapid evolution of the vortex tilt towards a quasi-equilibrium left-of-shear orientation. After the initial downshear tilting, the vortex in RWS3 oscillates about the left-of-shear direction, never departing from this orientation by more than 45°.

The PV amplitude and tilt direction from the heuristic model solution (14), using the values of ω_p and γ from Table 2, are also shown in Fig. 4. The net decay rate is used in place of the resonant damping rate in (14) since it is the *simulated* free-alignment decay that is relevant here. The peak amplitude value predicted by (14) should be most accurate (i.e., reproduce the simulated value) when the vortex closely approximates a single-core-plus-weak-skirt structure. While we have verified that this is indeed the case for the RWS vortices here (not shown), non-negligible quantitative differences in peak

---

RWS1 (not shown). In RWS3 the estimated value of γ_{cl} is more than double γ_{rad} so that the order-of-magnitude increase in γ from RWS1 to RWS3 is largely accounted for.

[4] Tilt evolution is depicted using PV in the forced experiments to parallel the heuristic model development in section 3a. Geopotential, which lacks the higher frequency oscillations evident in the PV field, is better suited for estimating the decay rate and precession frequency in the free-alignment experiments.

amplitude for the broader vortex of section 4 are found. Thus, for consistency, the peak amplitude from the heuristic model is scaled so as to match the initial peak simulated value for all experiments. Despite being based upon the approximate solution (8) using the vortex free-alignment response, the heuristic model describes extraordinarily well the simulated evolution of the tilt asymmetry. Effects related to the horizontal advection of the vertical shear-flow PV by the basic state vortex flow (i.e., the second term on the rhs of (11)) are, as discussed above, subdominant to the impacts of differential advection of basic state vortex PV by the vertical shear flow. At long times, the radial structure of the simulated PV perturbation is proportional to $d\overline{q}/dr$ (not shown), as anticipated by the heuristic model solution (14). Therefore, it follows that the enhanced resilience of the RWS2 and RWS3 sheared vortices can be attributed directly to the increased radial gradient of PV within the skirt and its impact on the resonant damping of the tilt mode.

When one considers the nature of the resonant damping mechanism, that damping occurs due to the resonance of a propagating core VRW with the surrounding flow at the critical radius of the core mode, it might at first sight seem surprising that the forced solution, which exhibits a time-dependant rate of phase propagation (Fig. 4), should be closely reproduced by a heuristic model invoking values of ω_p and γ based upon a constantly-propagating mode.

To gain a more complete understanding of the forced solution, we begin by examining the development of the linear critical layer. Figure 5a shows the azimuthal structure of the PV perturbation within a radial band centered on the estimated critical radius for the RWS3 free-alignment experiment. As basic state PV within the skirt is advected radially, the PV perturbation grows within the critical layer and perturbation

growth here is most effective near the location of the resonance. Conservation of global angular wave activity requires that the amplitude of the tilt mode must then decay (e.g., Schecter et al. 2002).

A similar illustration of the flow evolution is shown in Fig. 5b for the shear-forced RWS3 experiment. A critical layer appears to develop near the same radial location observed in the free-alignment experiment, suggesting that the resonant interaction of a constantly-propagating mode continues to play a role in the linear tilt evolution in the forced problem. The temporal evolution of the PV perturbation within the skirt in the shear-forced RWS3 experiment is shown in greater detail in Fig. 6. Over the duration of the simulation, the peak amplitude of the PV perturbation within the skirt grows. The corresponding decrease in the peak amplitude of the core tilt asymmetry (Fig. 4c) agrees qualitatively with the predictions of the resonant damping theory. The amplitude of the PV perturbation within the skirt, however, is modulated by the shear forcing just as it is in the core (Fig. 4c).

If the critical layer stirring were instead tied to the instantaneous rotation frequency of the shear-forced solution, one would expect to observe significant radial variation in the location of r_* with time. Except for a brief interval of time near 5 circulation periods, the estimated critical radius using the rotation frequency of the shear-forced solution lies outside 90-km radius at all times during the RWS3 simulation (not shown). The observed peak in PV perturbation amplitude within the skirt, by contrast, is consistently located near the value of r_* from the free-alignment simulation. Thus, we conclude that resonant damping in the linear shear-forced problem continues to be governed essentially by the intrinsic tilt mode identified in the free alignment experiment.

The heuristic model predicts that the amplitude of this rotating component eventually decays to zero, at which point resonant damping would cease. In this limit, the vortex has achieved an equilibrium tilt 90º left of shear.

4. "Cloudy Vortex" Experiments

When a TC encounters vertical wind shear, observations confirm that deep convection within the near-core region organizes into a distinctly asymmetric pattern with maximum ascent, precipitation, and lightning frequency downshear left (e.g., Reasor et al. 2000; Corbosiero and Molinari 2003; Reasor et al. 2013). Several plausible explanations have been put forth in the literature for how this occurs, but yet there is no clear consensus as to which mechanism is predominant. One set of theories argues that the balanced, adiabatic dynamics of the vortex-shear interaction determines regions favored for ascent. Diabatic heating is then organized within the envelope of upward mesoscale ascent in both conditionally stable and unstable environments (e.g., Davis et al. 2008; Riemer et al. 2010). The parameterization of heating in the system of equations (1)-(3) follows this conceptual view by assuming that the diabatic heating (cooling) is coupled to the asymmetric wavenumber-1 ascent (descent) associated with the dry vortex dynamics. The net effect of this coupling is to locally reduce the azimuthal-mean static stability within a radial band. A similar approach was taken by Patra (2004) in their examination of the convective heating's impact on the resilience of a sheared TC vortex.

Figure 7 shows the radial profiles of buoyancy reduction factor Y for the cloudy vortex experiments performed here. To establish the basic resilience properties of the observationally-based vortex, the first experiment, OBS1, involves no heating whatsoever

(i.e., $Y = 1$ everywhere). The remaining experiments specify $Y < 1$ at the outer edge of the core, r_c defined herein by the radius of maximum PV gradient. (This specification is consistent with the finding of Schecter and Montgomery (2007) using a non-hydrostatic mesoscale model that the minimum Y coincides with the maximum azimuthal-mean tangential wind.) In OBS2-4, the value of Y is progressively reduced locally and asymptotes to the OBS1 value within the "eye" and vortex skirt. Experiment OBS5 is similar, except Y is locally reduced to zero.

The free alignment of the vortex in each case, measured at r_c, is shown in Fig. 8a. Following the initial adjustment of the perturbation's radial structure in OBS1, as in the experiments of section 3, a clear exponential decay of the tilt asymmetry is observed. The critical radius $r_* \approx 3r_c$ in this case (Table 2). The local reduction of static stability in OBS2 and OBS3 results in an increase in the value of ω_p and corresponding inward shift of r_*. Also, γ in OBS2 (OBS3) is more than a factor of two (three) larger than in OBS1. A further reduction of the local static stability to near-neutral values in OBS4 results in a tilt asymmetry decay that is not clearly exponential. When the tilt asymmetry is measured instead at r = 40 km, radially outside the region of peak heating, exponential decay is observed in OBS4 following the initial adjustment (Fig. 8b) at a rate five times larger than in OBS1. The different solution behavior inside and outside the heating region for large reductions of static stability suggests that tilt defined via conventional methods like PV centroid will have a strong radial scale dependence in the TC. In OBS5, where the static stability is reduced locally to zero, exponential decay of the tilt asymmetry is not readily observed within or radially outside the region of heating. Without employing the previously-noted semi-analytical methods for computing the precession frequency and

damping rate, the contribution of the tilt mode to the tilt asymmetry evolution cannot be clarified in this limiting case. Here it is not essential that the weak excitation of the tilt mode be fully quantified. We refer the reader to a recent study by Schecter (2015) which examines the issue of tilt mode excitation in the context of convection-permitting TC simulations.

The observation-based vortex is next subjected to unidirectional shear with U = -2.75 m s^{-1}, yielding 5.5 m s^{-1} of deep-layer westerly shear. Figure 9 shows the PV perturbation amplitude measured at r_c (with the exception of OBS4-5, where it is measured at r = 40 km) and the direction of tilt in each case. For reference, 1 circulation period is equivalent to ~45 min. Within a few circulation periods the tilt asymmetry in OBS1 (Fig. 9a) approaches a quasi-equilibrium configuration in which the tilt direction varies by no more than 45° from the left-of-shear direction and the tilt amplitude gradually asymptotes to a steady value. This long-term resistance to shearing reinforces the idea promoted by RMG04 and Jones (2004) that mechanisms intrinsic to the adiabatic dynamics are capable of maintaining the vertical alignment of a TC-like vortex on meteorologically-relevant timescales[5]. Furthermore, the close agreement between the simulated and heuristic model solutions supports the relevance of the resonant damping mechanism to vortices more closely resembling TCs. The simulated solution shows higher-frequency harmonics and a growing departure from the heuristic model solution with time. These harmonics are not evident in the RWS cases of section 3, indicating that

[5] Whether the vortex is able to survive the initial tilting in the fully nonlinear problem is not formally addressed here. RMG04 argued that a necessary condition required for the vortex to resist the shearing is revealed by comparing the free-alignment value of ω_p to the differential advection rate, $\tau_s^{-1} \sim U/L$. According to this perspective, a vortex will tend to remain vertically coherent when the intrinsic precession frequency exceeds τ_s^{-1}. For the OBS experiments, $\tau_s^{-1} \approx 10^{-4}$ s^{-1}. Since ω_p is at least a factor of 5 larger in each of the OBS cases, we may anticipate a nonlinearly resilient vortex.

some assumptions and approximations of the single-core-plus-weak-skirt heuristic model start to become tenuous for broader radial distributions of PV.

The shear-forced tilt asymmetries in OBS2 (Fig. 9b) and OBS3 (Fig. 9c) with moderate local reduction of Y behave similarly to that in the no-heating experiment OBS1. As anticipated from the discussion summarized in the Introduction, the resonant damping is enhanced through the local reduction in Rossby deformation radius and inward shifting of the critical radius to a region of greater PV gradient. As a consequence, the vortex achieves the quasi-equilibrium tilt configuration over a shorter time period and with smaller final tilt magnitude than without heating.

In OBS4 (Fig. 9d) and OBS5 (Fig. 9e) the shear-forced vortex evolution for the transition to locally neutral static stability values in the core is examined. Because the free-alignment solution shows little evidence of damped-mode behavior within the region of peak heating in these cases, the tilt magnitude and direction are instead measured outside the region of heating at the outer edge of the core. In contrast to the evolution in OBS1-3, the tilt magnitude in OBS4 almost immediately exhibits high-frequency, constant-amplitude oscillations about a quasi-equilibrium value. The tilt direction behaves similarly. Note, however, that the longer-timescale variations in magnitude and direction predicted by the heuristic model over the first 10 circulation periods are still reflected in the simulated solution. The differences between the simulated tilt evolution in OBS4 and OBS5 are subtle. Due to our inability to theoretically estimate ω_p and γ in the OBS5 free-alignment case, we simply reproduce the heuristic model solution from OBS4 in Fig. 9e as an approximation. As in OBS4, the simulated solution continues to reflect the longer-time oscillations in tilt magnitude and direction from the heuristic model.

Further insight into the impact of heating on the shear-forced tilt is obtained by comparing the PV and vertical velocity perturbation structure from OBS1 (Fig. 10) with that from OBS5 (Fig. 11) at select times during the early evolution. Only the ascending contribution to the wavenumber-1 vertical motion asymmetry is shown for clarity. Differential advection of the symmetric vortex by the vertical shear flow at early times produces a broad-scale PV dipole in the direction of the imposed shear vector (Fig. 10a and 11a). According to balance arguments of Jones (1995), ascent (descent) is initially produced downshear (upshear) as the vortex attempts to maintain thermal wind balance on account of the tilted wind field. Since the parameterized diabatic heating is proportional to the vertical motion, it can be readily shown using the definition of PV perturbation for the Boussinesq system linearized about a barotropic mean vortex,

$$q' = N^2\zeta' + \overline{\eta}\,\frac{\partial^2\phi'}{\partial z^2}\,, \tag{16}$$

and the incompressible mass continuity equation,

$$\frac{1}{r}\frac{\partial(ru')}{\partial r} + \frac{1}{r}\frac{\partial v'}{\partial \varphi} + \frac{\partial w'}{\partial z} = 0\,, \tag{17}$$

that the diabatic generation of PV for the linearized system (1)-(3) is proportional to

$$\frac{\partial q'}{\partial t} \propto \left[1 - Y(r)\right] N^2 \overline{\eta}\,\frac{\partial w'}{\partial z}. \tag{18}$$

Thus, within the “eyewall” region of lowest Y in OBS5, positive (negative) PV perturbation is generated downshear (upshear) at low levels as can be inferred from Fig. 11a. The diabatic generation of PV perturbation occurs within the system-scale tilt asymmetry produced by differential advection, effectively splitting the initial tilt asymmetry.

The subsequent vortex tilt evolution is readily discerned in the dry limit configuration of OBS1 given the discrete structure of the PV asymmetry throughout the domain. As the tilt rotates cyclonically and increases in magnitude, the peak ascent in OBS1 shifts to the right-of-tilt direction and maintains this orientation as the tilt oscillates about the left-of-shear direction (Fig. 10b-d). Jones (1995) described this phase relationship between the vertical motion asymmetry and tilt as the balanced-dynamical response of vortex flow moving over the distorted isentropes of the tilted vortex. The significant local reduction of azimuthal-mean static stability in OBS5 yields a more complex PV and vertical motion structure within the core region following the initial vortex tilting (Fig. 11b-d). Inside the moist-neutral "eyewall" region from 24- to 28-km radius, the PV perturbation is comprised of fine-scale banded structures. Animations of these features indicate that they retrogress, propagating clockwise (not shown). The vortex tilt on this sub-vortex scale is difficult to assess in OBS5 without employing some quantitative method (e.g., PV centroid). In contrast, on the broader system scale, beyond 30-km radius, the PV asymmetry structure strongly resembles that in OBS1 and suggests a left-of-shear tilt. Additionally, an envelope of ascent[6] near 30-km radius appears oriented in the right-of-tilt direction, as in OBS1, but is more confined radially. A persistent PV asymmetry that is approximately 180° out of phase with the near-core tilt asymmetry just outside the peak heating radius (r = 28 km), is likely generated and maintained by the heating within this envelope.

[6] Peak values of diagnosed ascent inside the region of greatest heating exceed 40 ms^{-1} in OBS5. The PV perturbation also exhibits local values there that are an order of magnitude larger than found in OBS1. In the localized region where $YN^2 \rightarrow 0$, these values indicate that the limits of the hydrostatic model may have been reached. Consequently, the solution there must be approached with caution.

5. Discussion and Conclusions

According to the linear heuristic model of RMG04 for a TC-like vortex that is immersed in a sustained unidirectional vertical shear flow, the rate at which a vortex asymptotes to the equilibrium configuration, and hence its resilience, is a function of the *intrinsic* decay rate of the core-tilt mode, which, in the absence of amplification through frequency-matched IGW radiation, is proportional to the mean radial PV gradient within the vortex skirt. In the context of dry "adiabatic" linearized dynamics, idealized numerical solutions are shown to confirm that an increase in the radial gradient of PV within the vortex skirt surrounding the core yields a more rapid evolution of a sheared vortex towards a quasi-equilibrium, left-of-shear tilt configuration.

To further assess the strengths and weaknesses of the heuristic model in the more realistic case of a *cloudy vortex* in unidirectional shear, a simple parameterization of latent heating in the core region is employed based on prior work. For modest reductions of the azimuthal-mean static stability within the core, the heuristic model continues to provide a consistent picture of the simulated vortex evolution and its sensitivities. However, in the limit of strictly moist-neutral dynamics within a narrow region of the "eyewall", the heuristic model yields a poor approximation to the simulated vortex evolution within the region of peak heating, but a left-of-shear tilt of the near-core vortex, radially beyond the heating region, remains the preferred long-time solution.

The foregoing findings naturally motivate the following question: *Is the heuristic model still applicable to the vortex tilt evolution in the limit of moist-neutral dynamics, and, if so, in what sense?*

To help answer this question, Fig. 12 summarizes the transition in shear-forced asymmetry evolution from the limit of no heating (OBS1, Fig. 12a) to the limit of zero moist stability (OBS5, Fig. 12d) within the core. Consistent with our analysis in section 4, the PV perturbation in OBS1 (Fig. 12a) clearly indicates the presence of a forced, damped tilt mode with an amplitude that peaks in the core and decays radially within the skirt. Careful examination of these solutions shows also radially-outward propagating features. Reasor and Montgomery (2001) identified similar outward-propagating features in the free-alignment context as trailing spiral VRWs. Since the tilt quasimode solution resides in the continuous spectrum, it must ultimately decay through the "leaking" of energy via the radial propagation of these VRWs. They noted that nonlinear advection tends to counteract the VRW dispersion. When the static stability is halved locally (OBS2, Fig. 12b), the forced modal structure is still evident, but the outward energy propagation is more prominent in the solution. For small, but non-zero, local values of static stability (OBS4, Fig. 12c), the presence of a forced mode is not readily discerned in the core. Instead, the PV perturbation amplitude peaks where the heating is maximized (r ~ 28 km). In the limit of locally neutral (zero) static stability (OBS5, Fig. 12d), a similar, but larger-amplitude and more radially confined PV perturbation is evident near the radius of peak heating. This amplitude maximum, observed for small values of local static stability, is tied to the vortex tilt and is likely generated and maintained by the heating there. Unique to the moist-neutral limit, a second and distinct region of large-amplitude PV asymmetry exists radially inside the heating maximum. As fine-scale banded features develop here (see Fig. 11), Fig. 12d shows that the PV perturbation maintains its large amplitude. Nonlinear dynamics may become important in this

"eyewall" region, requiring a future modification of the linear theory. In both OBS4 and OBS5 a PV maximum outside 30-km radius is associated with the trailing spiral VRWs at the outer edge of the core.

The timing and outward-propagation speed of the VRWs are similar in all OBS simulations. Comparison of the simulated solution to the heuristic model solution in section 4 reveals that a tilt mode continues to govern the longer-time evolution of vortex tilt *outside* the core in OBS4 and likely in OBS5. Thus, while the simulated linear primitive equation solution outside the heating region exhibits continuous-spectrum type VRW characteristics, the tilt evolution in this part of the near-core region is still meaningfully described by a shear-forced discrete tilt mode. An assessment of whether the tilt mode is forced at all near the core radius r_c requires the application of semi-analytical methods, as in Schecter et al. (2002), which we reserve for future work.

Acknowledgments.

The first author (PDR) would like to acknowledge support from NSF ATM-0514199. Both authors would like to thank Dr. David Schecter for stimulating discussions that helped motivate this study and for his insightful comments on the manuscript, including that which motivated Eq. (15). We would also like to thank two anonymous reviewers for their substantive comments, which have helped clarify both thought and presentation. The second author (MTM) would like to acknowledge support from NSF AGS-0733380, AGS-1313948, NOAA's Hurricane Research Division and the U.S. Naval Postgraduate School.

References

Briggs, R. J., J. D. Daugherty, and R. H. Levy, 1970: Role of Landau damping in crossed-field electron beams and inviscid shear flow. *Phys. Fluids*, **13**, 421–432.

Corbosiero, K. L. and J. Molinari, 2003: The relationship between storm motion, vertical wind shear, and convective asymmetries in tropical cyclones. *J. Atmos. Sci.*, **60**, 366–376.

Davis, C. A., S. C. Jones, and M. Riemer, 2008: Hurricane vortex dynamics during Atlantic extratropical transition. *J. Atmos. Sci.*, **65**, 714–736.

Durran, D. R. and J. B. Klemp, 1982: On the effects of moisture on the Brunt-Väisälä frequency. *J. Atmos. Sci.*, **39**, 2152-2158.

Emanuel, K. A., M. Fantini, and A. J. Thorpe, 1987: Baroclinic instability in an environment of small stability to slantwise moist convection. Part I: Two-dimensional models. *J. Atmos. Sci.*, **44**, 1559–1573.

Emanuel, K., C. DesAutels, C. Holloway, and R. Korty, 2004: Environmental control of tropical cyclone intensity. *J. Atmos. Sci.*, **61**, 843–858.

Hoskins, B. J., and F. P. Bretherton, 1972: Atmospheric frontogenesis models: Mathematical formulation and solution. *J. Atmos. Sci.*, **29**, 11–37.

Jones, S. C., 1995: The evolution of vortices in vertical shear. I: Initially barotropic vortices, *Quart. J. Roy. Meteor. Soc.*, **121**, 821–851.

Jones, S. C., 2004: On the ability of dry tropical-cyclone-like vortices to withstand vertical shear. *J. Atmos. Sci.*, **61**, 114–119.

Kimball, S. K., 2006: A modeling study of hurricane landfall in a dry environment. *Mon. Wea. Rev.*, **134**, 1901–1918.

Mallen, K. J., M. T. Montgomery, and B. Wang, 2005: Reexamining the near-core radial structure of the tropical cyclone primary circulation: Implications for vortex resiliency. *J. Atmos. Sci*., **62**, 408–425.

McWilliams, J. C., L. P. Graves, and M. T. Montgomery, 2003: A formal theory for vortex Rossby waves and vortex evolution. *Geophys. Astrophys. Fluid Dyn.*, **97**, 275–309.

Melander, M. V., J. C. McWilliams, and N. J. Zabusky, 1987: Axisymmetrization and vortex gradient intensification of an isolated two-dimensional vortex through filamentation. *J. Fluid Mech.*, **178**, 137–159.

Montgomery, M. T., and R. J. Kallenbach, 1997: A theory for vortex Rossby-waves and its application to spiral bands and intensity changes in hurricanes. *Quart. J. Roy. Meteor. Soc.*, **123**, 435–465.

Nolan, D. S., M. T. Montgomery, and L. D. Grasso, 2001: The wavenumber-one instability and trochoidal motion of hurricane-like vortices. *J. Atmos. Sci.*, **58**, 3243–3270.

Päschke, E., P. Marschalik, A. Z. Owinoh and R. Klein, 2012: Motion and structure of atmospheric mesoscale baroclinic vortices: dry air and weak environmental shear. *J. Fluid Mech.*, **701**, 137-170.

Patra, R., 2004: Idealized modeling of tropical cyclones in vertical shear: The role of saturated ascent in the inner core. Preprints, *26th Conf. on Hurricanes and Tropical Meteorology*, Miami, FL, Amer. Meteor. Soc., 98–99.

Reasor, P. D., M. T. Montgomery, F. D. Marks Jr., and J. F. Gamache, 2000: Low-wavenumber structure and evolution of the hurricane inner core observed by airborne dual-Doppler radar. *Mon. Wea. Rev.*, **128**, 1653-1680.

Reasor, P. D. and M. T. Montgomery, 2001: Three-dimensional alignment and corotation of weak, TC-like vortices via linear vortex Rossby waves. *J. Atmos. Sci.*, **58**, 2306–2330.

Reasor, P. D., M. T. Montgomery, and L. D. Grasso, 2004: A new look at the problem of tropical cyclones in vertical shear flow: Vortex resiliency, *J. Atmos. Sci.*, **61**, 3–22.

Reasor, P. D., and M. D. Eastin, 2012: Rapidly intensifying Hurricane Guillermo (1997). Part II: Resilience in shear. *Mon. Wea. Rev.*, **140**, 425–444.

Reasor, P.D., R. Rogers, and S. Lorsolo, 2013: Environmental flow impacts on tropical cyclone structure diagnosed from airborne Doppler radar composites. *Mon. Wea. Rev.*, **141**, 2949–2969.

Riemer, M., M. T. Montgomery, and M. E. Nicholls, 2010: A new paradigm for intensity modification of tropical cyclones: thermodynamic impact of vertical wind shear on the inflow layer. *Atmos. Chem. Phys.*, **10**, 3163–3188.

Riemer, M., and M. T. Montgomery, 2011: Simple kinematic models for the environmental interaction of tropical cyclones in vertical wind shear. *Atmos. Chem. Phys.*, **11**, 9395–9414.

Riemer, M., M. T. Montgomery, and M. E. Nicholls, 2013: Further examination of the thermodynamic modification of the inflow layer of tropical cyclones by vertical wind shear. *Atmos. Chem. Phys.*, **13**, 327–346.

Schecter, D. A., M. T. Montgomery, and P. D. Reasor, 2002: A theory for the vertical alignment of a quasigeostrophic vortex. *J. Atmos. Sci.*, **59,** 150–168.

Schecter, D. A., and M. T. Montgomery, 2003: On the symmetrization rate of an intense geophysical vortex. *Dyn. Atmos. Oceans*, **37,** 55–87.

Schecter, D. A., and M. T. Montgomery, 2004: Damping and pumping of a vortex Rossby wave in a monotonic cyclone: Critical layer stirring versus inertia-buoyancy wave emission. *Phys. Fluids*, **16,** 1334–1348.

Schecter, D. A., and M. T. Montgomery, 2006: Conditions that inhibit the spontaneous radiation of spiral inertia–gravity waves from an intense mesoscale cyclone. *J. Atmos. Sci.*, **63,** 435–456.

Schecter, D. A., and M. T. Montgomery, 2007: Waves in a cloudy vortex. *J. Atmos. Sci.*, **64,** 314–337.

Schecter, D. A., 2015: Response of a simulated hurricane to misalignment forcing compared to the predictions of a simple theory. *J. Atmos. Sci.*, in press.

Schubert, W. H., M. T. Montgomery, R. K. Taft, T. A. Guinn, S. R. Fulton, J. P. Kossin, and J. P. Edwards, 1999: Polygonal eyewalls, asymmetric eye contraction, and potential vorticity mixing in hurricanes. *J. Atmos. Sci*, **56**, 1197-1223.

Simpson, R. H. and H. Riehl, 1958: Mid-tropospheric ventilation as a constraint on hurricane development and maintenance. *Proc. Tech. Conf. on Hurricanes*, Miami, FL, Amer. Meteor. Soc., D4.1-D4.10.

Smith, G. B., and M. T. Montgomery, 1995: Vortex axisymmetrization: Dependence on azimuthal wave-number or asymmetric radial structure changes. *Quart. J. Roy. Meteor. Soc.*, **121**, 1615–1650.

Tang, B., and K. Emanuel, 2010: Midlevel ventilation's constraint on tropical cyclone intensity. *J. Atmos. Sci.*, **67**, 1817–1830.

Tang, B., K. Emanuel, 2012: Sensitivity of tropical cyclone intensity to ventilation in an axisymmetric model. *J. Atmos. Sci.*, **69**, 2394–2413.

List of Figures

FIG. 1. Illustration of the core and skirt regions of an idealized tropical cyclone-like vortex. The region of greatest PV is bounded by the core radius r_c, and is surrounded by a skirt of much smaller PV. Here, r_c is defined as the radius of maximum PV gradient. The core may support a discrete vortex-Rossby wave which resonates with the surrounding flow at the critical radius r_*. Adapted from Fig. 2 of Schecter et al. (2002).

FIG. 2. The azimuthal-mean vortex used in (a) RWS1 (solid), RWS2 (dashed) and RWS3 (dotted), and in (b) OBS1-5. The inset in (a) shows the radial profile of relative vertical vorticity within the vortex skirt, highlighting differences in the corresponding radial gradient. For the equivalent barotropic system, the azimuthal-mean PV is related to the relative vorticity by $\bar{q} = N^2\left(f + \bar{\zeta}\right)$.

FIG. 3. Vortex alignment as a function of skirt PV gradient. Log-linear plot shows the core VRW geopotential amplitude evaluated at the core radius r_c as a function of time for RWS1 (thick solid), RWS2 (dashed) and RWS3 (dotted). The light solid gray lines indicate linear best fits to the data in each case. Time is in units of circulation period at r_c; $|\phi_1|_{\max}$ is the maximum value of the geopotential perturbation over each simulation.

FIG. 4. Tilt amplitude and direction in the shear-forced (a) RWS1, (b) RWS2 and (c) RWS3 experiments. Tilt amplitude is measured by the PV perturbation (s^{-3}) at the core radius r_c (top). Tilt direction is defined as the crest azimuth of the PV perturbation at $z = H$ (bottom). The solid lines show the simulated solution to the primitive equation model of section 2, and the dashed lines show the heuristic model approximation to it using the decay rate and precession frequency from the respective free-alignment simulations. The heuristic model amplitude is scaled so as to match the initial peak-simulated value. 90º

represents the left-of-shear direction, the equilibrium-tilt direction of the sheared vortex in all cases. Time is in units of circulation period at r_c.

FIG. 5. The development of the linear critical layer in RWS3. Shown is the PV perturbation evolution (from left to right) within the vortex skirt for the (a) free-alignment and (b) sheared-forced cases. The dashed line indicates the location of the critical radius r_* in the free-alignment experiment. Here, $q_{1,\max}$ is the maximum PV perturbation over the entire domain and over the duration of each simulation (i.e., the peak core VRW amplitude). Time is in units of circulation period at the core radius r_c.

FIG. 6. Temporal evolution of PV perturbation amplitude within the vortex skirt in the shear-forced RWS3 experiment. The dashed line indicates the location of the critical radius r_* in the corresponding free-alignment experiment. The modulation of disturbance PV amplitude within the skirt occurs as a result of the shear forcing. Here, $|q_1|_{\max}$ is the maximum PV perturbation over the entire domain and over the duration of the simulation (i.e., the peak core VRW amplitude). Time is in units of circulation period at the core radius r_c.

FIG. 7. Radial profiles of the buoyancy reduction factor, Y for OBS1 (solid red), OBS2 (dotted), OBS3 (dashed), OBS4 (dash-dot), and OBS5 (solid black). For reference, the heavy solid line shows the relative vorticity profile of the azimuthal-mean vortex. In the experiments with heating, the effective static stability is reduced at the edge of the vortex core and approaches rapidly a typical “environmental” value away from the region of strongest tangential wind.

FIG. 8. Vortex alignment as a function of effective static stability. Log-linear plot shows the geopotential amplitude as a function of time for OBS1 (solid red), OBS2 (dotted),

OBS3 (dashed), OBS4 (dash-dot), and OBS5 (solid black). In (a) the asymmetry amplitude is measured at the core radius r_c. In (b) the asymmetry is sampled at r = 40 km, radially outside the region of peak heating (cf. Fig. 7). The light solid gray lines indicate linear best fits to the data in each case. Time is in units of circulation period at r_c; $|\phi_1|_{\max}$ is the maximum value of the geopotential perturbation over each simulation.

FIG. 9. Tilt amplitude and direction in the shear-forced (a) OBS1, (b) OBS2, (c) OBS3, (d) OBS4, and (e) OBS5 experiments. Tilt amplitude (top) is measured by the PV perturbation (s^{-3}) at the core radius r_c in OBS1-3 and at r = 40 km, radially outside the region of peak heating (cf. Fig. 7), in OBS4-5. Tilt direction is defined as the crest azimuth of the PV perturbation at $z = H$ (bottom). The solid lines show the simulated solution to the primitive equation model of Section 2, and the dashed lines show the heuristic model approximation to it using the decay rate and precession frequency from the respective free-alignment simulations. The heuristic model amplitude is scaled so as to match the initial peak-simulated value. Because the precession frequency and decay rate cannot be meaningfully estimated from the free-alignment solution in OBS5, values from OBS4 are used in the heuristic model solution in (e). 90º represents the left-of-shear direction, the equilibrium-tilt direction of the sheared vortex in all cases. Time is in units of circulation period at r_c.

FIG. 10. Time evolution of core region PV perturbation (shaded, at z = 0) and positive vertical motion perturbation (at $z = H/2$) contoured at 0.25, 0.5, 0.75, and 1.5 ms^{-1} for the shear-forced OBS1 experiment. Vertical wind shear, indicated by the arrow in the top-left panel, is directed to the right. The fields are shown at (a) 0.25, (b) 1.5, (c) 2, and (d) 5 circulation periods. The early downshear-tilted vortex corresponds to a PV dipole with

positive (negative) perturbation values upshear (downshear) at low levels. The horizontal scale is in km.

FIG. 11. As in Fig. 10, but for OBS5. Peak values of vertical motion and PV perturbation within the core exceed the contour ranges used in Fig. 10. To facilitate comparison of structure outside the core, the contour levels used in Fig. 10 are still employed here. See text for further discussion.

FIG. 12. Temporal evolution of the logarithmically-scaled PV amplitude within the core region in the shear-forced (a) OBS1, (b) OBS2, (c) OBS4, and (d) OBS5 experiments. Time is in units of circulation period at the core radius r_c.

TABLE 1. Description of the experiments performed for this study. The Rankine-with-skirt (RWS) and observation-based (OBS) vortex profiles are shown in Fig. 2. See text for the definition of the buoyancy reduction factor, *Y*.

Experiment	Vortex Profile	Heating (min *Y*)
RWS1	RWS: Skirt PV gradient, control	No (1)
RWS2	", ↑ 33%	No (1)
RWS3	", ↑ 100%	No (1)
OBS1	Observation-based PV monopole	No (1)
OBS2	“	Yes (0.5)
OBS3	“	Yes (0.25)
OBS4	“	Yes (0.0625)
OBS5	“	Yes (0)

TABLE 2. Estimated vortex core radius r_c, resonant damping critical radius r_*, net decay rate γ, and core VRW precession frequency ω_p for each experiment. The net decay rate and precession frequency are evaluated at r_c, except in OBS4-5 where they are evaluated radially outside the region of peak heating at r = 40 km. The simulated net decay rate is the sum of the (negative) resonant damping rate and (positive) inertia-gravity wave pumping rate. See text for further details. Because the amplitude decay in OBS5 is not clearly exponential in time following the initial adjustment period (cf. Fig. 8), the flagged values ( )† are only tenuously associated with resonant damping.

Experiment	Core Radius r_c (km)	Critical Radius r_* (km)	Net Decay Rate γ (10^{-5} s^{-1})	Precession Frequency ω_p (10^{-4} s^{-1})
RWS1/2/3	30	69/69/68.5	-0.10/0.61/1.69	2.61/2.64/2.70
OBS1/2/3	23	66.5/64.25/62.75	-1.97/4.27/6.41	5.48/5.85/6.13
OBS4	23	61.5	-10.52	6.39
OBS5	23	(29)†	(-5.20)†	(22.51)†

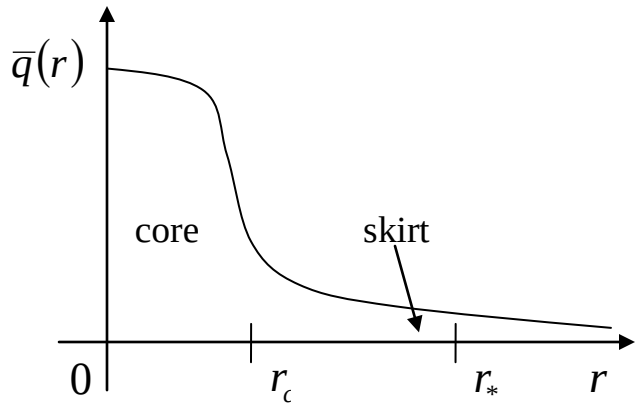

FIG. 1. Illustration of the core and skirt regions of an idealized tropical cyclone-like vortex. The region of greatest PV is bounded by the core radius r_c, and is surrounded by a skirt of much smaller PV. Here, r_c is defined as the radius of maximum PV gradient. The core may support a discrete vortex-Rossby wave which resonates with the surrounding flow at the critical radius r_*. Adapted from Fig. 2 of Schecter et al. (2002).

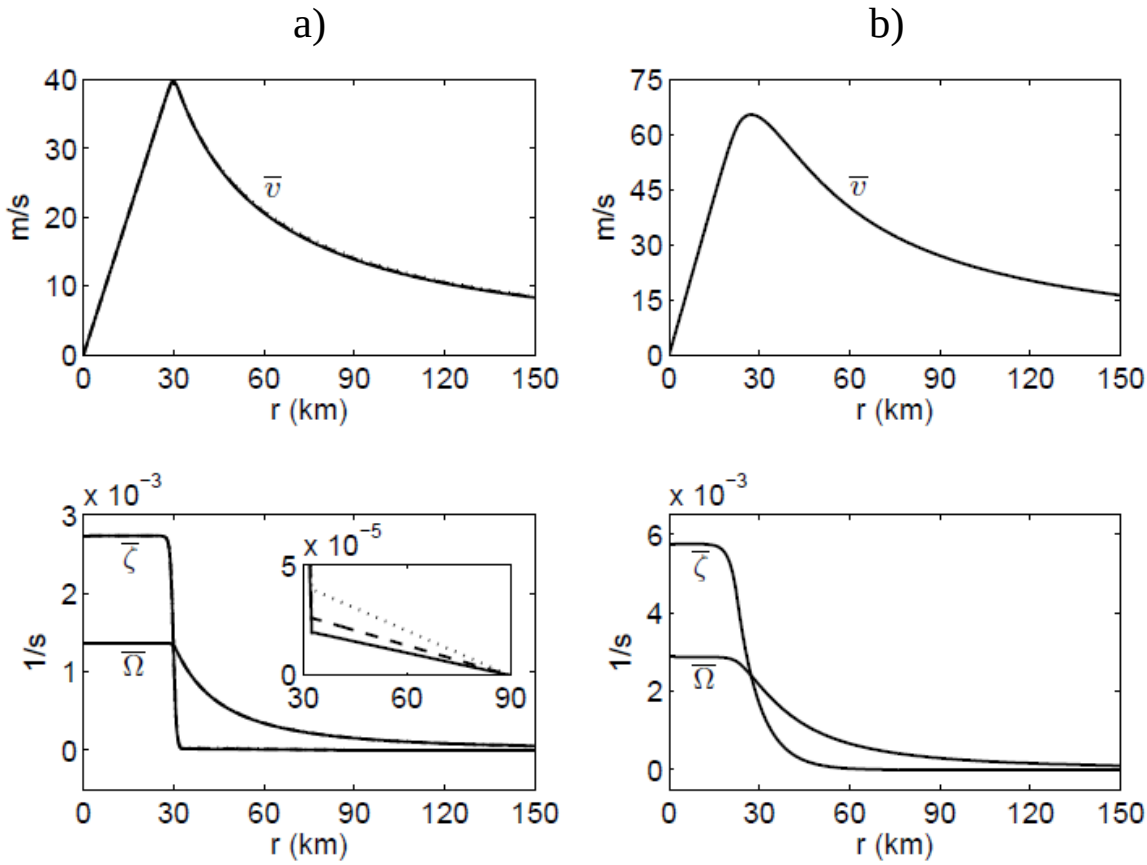

FIG. 2. The azimuthal-mean vortex used in (a) RWS1 (solid), RWS2 (dashed) and RWS3 (dotted), and in (b) OBS1-5. The inset in (a) shows the radial profile of relative vertical vorticity within the vortex skirt, highlighting differences in the corresponding radial gradient. For the equivalent barotropic system, the azimuthal-mean PV is related to the relative vorticity by $\overline{q} = N^2\left(f + \overline{\zeta}\right)$.

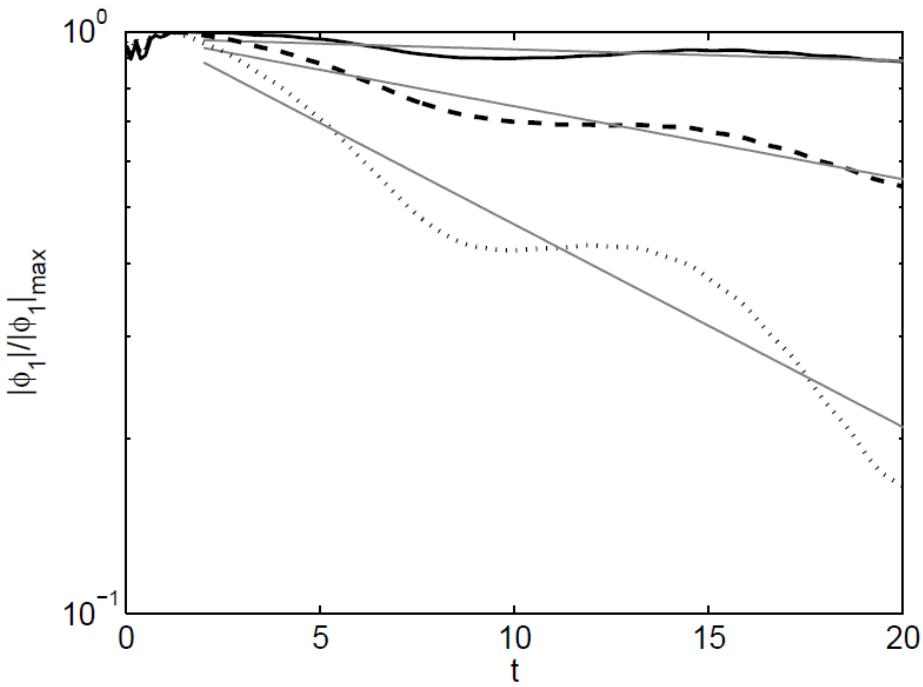

FIG. 3. Vortex alignment as a function of skirt PV gradient. Log-linear plot shows the core VRW geopotential amplitude evaluated at the core radius r_c as a function of time for RWS1 (thick solid), RWS2 (dashed) and RWS3 (dotted). The light solid gray lines indicate linear best fits to the data in each case. Time is in units of circulation period at r_c; $|\phi_1|_{\max}$ is the maximum value of the geopotential perturbation over each simulation.

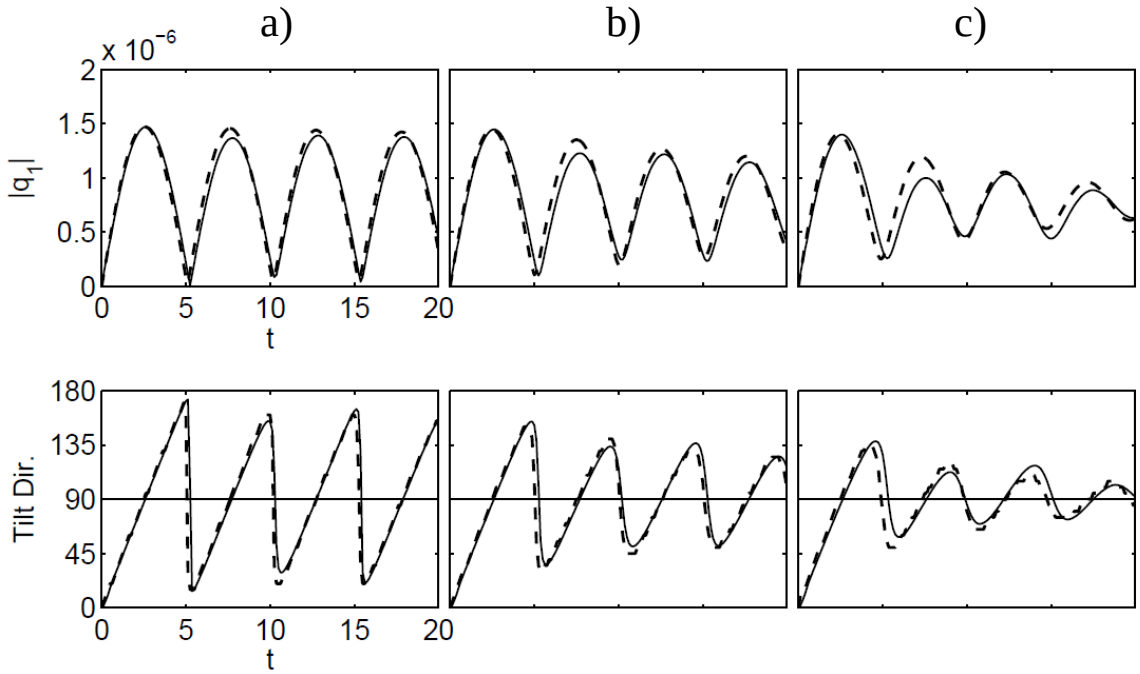

FIG. 4. Tilt amplitude and direction in the shear-forced (a) RWS1, (b) RWS2 and (c) RWS3 experiments. Tilt amplitude is measured by the PV perturbation (s^{-3}) at the core radius r_c (top). Tilt direction is defined as the crest azimuth of the PV perturbation at $z = H$ (bottom). The solid lines show the simulated solution to the primitive equation model of section 2, and the dashed lines show the heuristic model approximation to it using the decay rate and precession frequency from the respective free-alignment simulations. The heuristic model amplitude is scaled so as to match the initial peak-simulated value. 90º represents the left-of-shear direction, the equilibrium-tilt direction of the sheared vortex in all cases. Time is in units of circulation period at r_c.

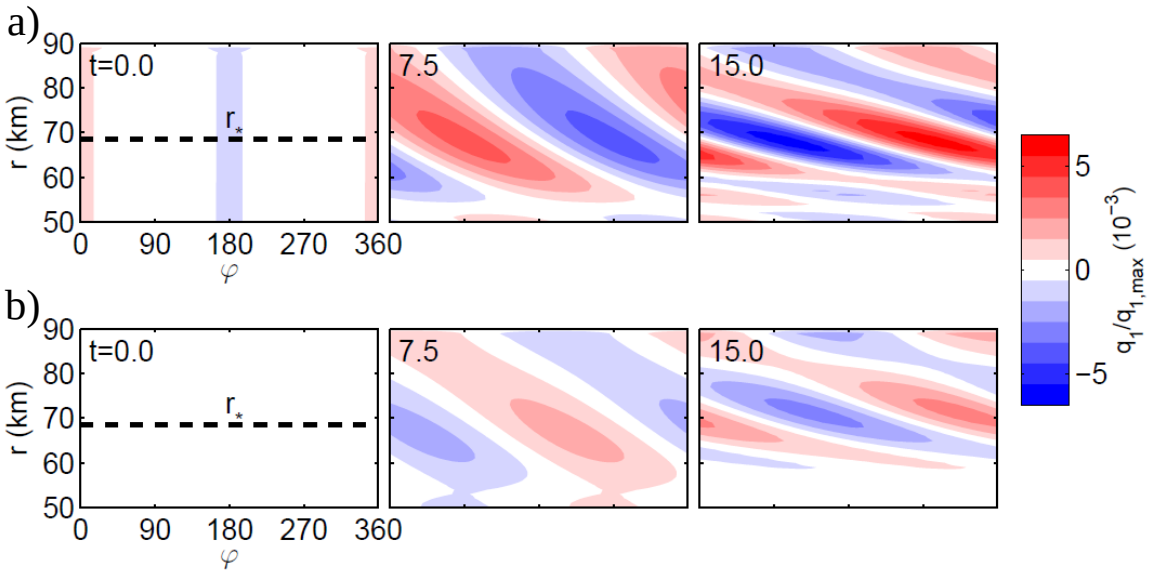

FIG. 5. The development of the linear critical layer in RWS3. Shown is the PV perturbation evolution (from left to right) within the vortex skirt for the (a) free-alignment and (b) sheared-forced cases. The dashed line indicates the location of the critical radius r_* in the free-alignment experiment. Here, $q_{1,\max}$ is the maximum PV perturbation over the entire domain and over the duration of each simulation (i.e., the peak core VRW amplitude). Time is in units of circulation period at the core radius r_c.

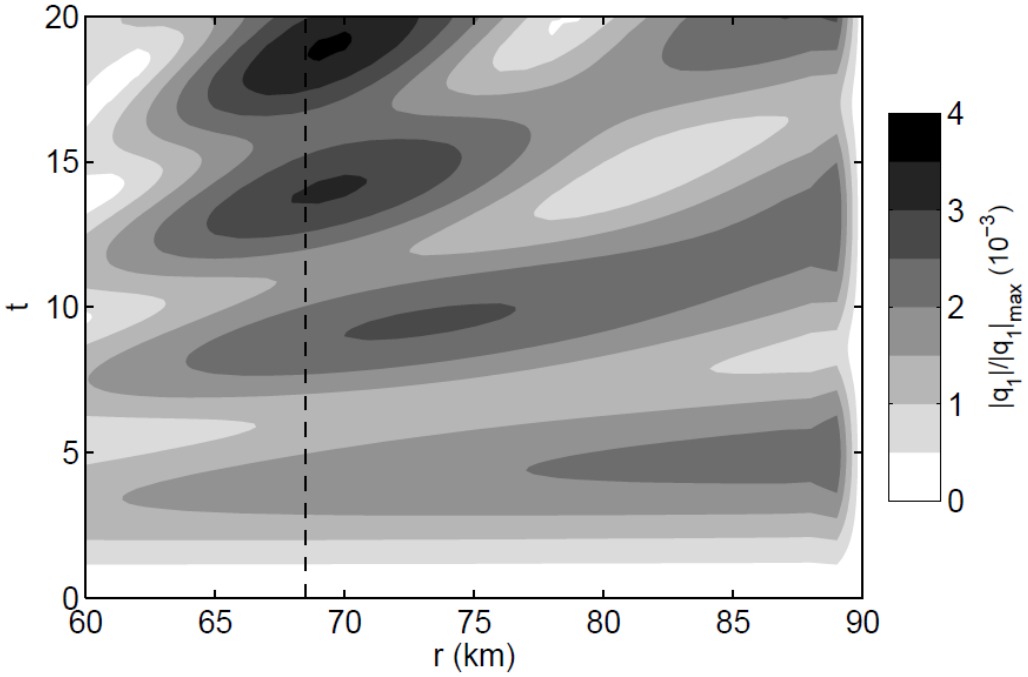

FIG. 6. Temporal evolution of PV perturbation amplitude within the vortex skirt in the shear-forced RWS3 experiment. The dashed line indicates the location of the critical radius r_* in the corresponding free-alignment experiment. The modulation of disturbance PV amplitude within the skirt occurs as a result of the shear forcing. Here, $|q_1|_{\max}$ is the maximum PV perturbation over the entire domain and over the duration of the simulation (i.e., the peak core VRW amplitude). Time is in units of circulation period at the core radius r_c.

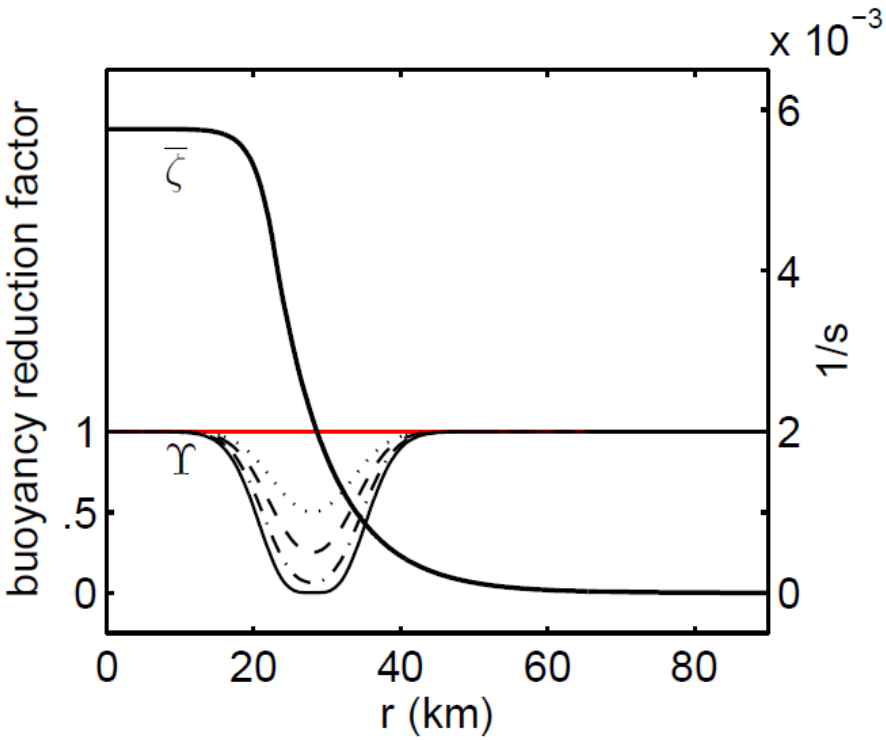

FIG. 7. Radial profiles of the buoyancy reduction factor, *Y* for OBS1 (solid red), OBS2 (dotted), OBS3 (dashed), OBS4 (dash-dot), and OBS5 (solid black). For reference, the heavy solid line shows the relative vorticity profile of the azimuthal-mean vortex. In the experiments with heating, the effective static stability is reduced at the edge of the vortex core and approaches rapidly a typical "environmental" value away from the region of strongest tangential wind.

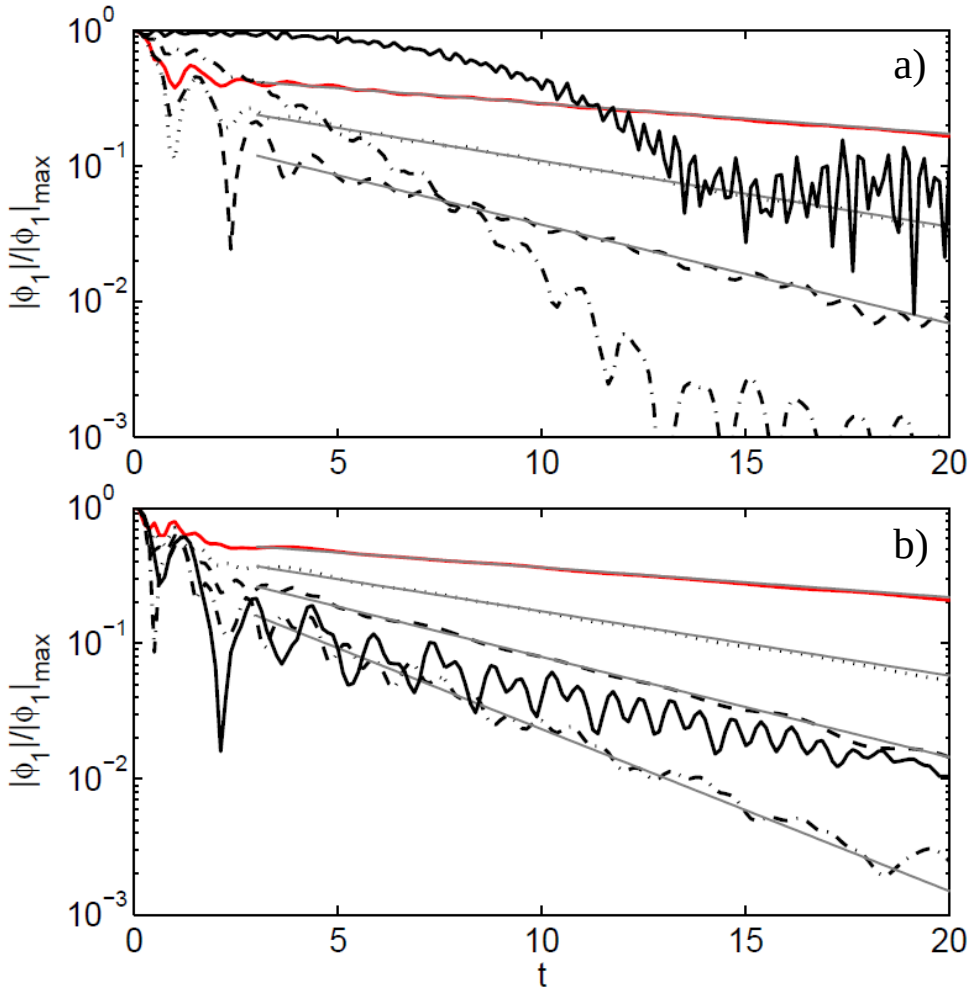

FIG. 8. Vortex alignment as a function of effective static stability. Log-linear plot shows the geopotential amplitude as a function of time for OBS1 (solid red), OBS2 (dotted), OBS3 (dashed), OBS4 (dash-dot), and OBS5 (solid black). In (a) the asymmetry amplitude is measured at the core radius r_c. In (b) the asymmetry is sampled at r = 40 km, radially outside the region of peak heating (cf. Fig. 7). The light solid gray lines indicate linear best fits to the data in each case. Time is in units of circulation period at r_c; $|\phi_1|_{\max}$ is the maximum value of the geopotential perturbation over each simulation.

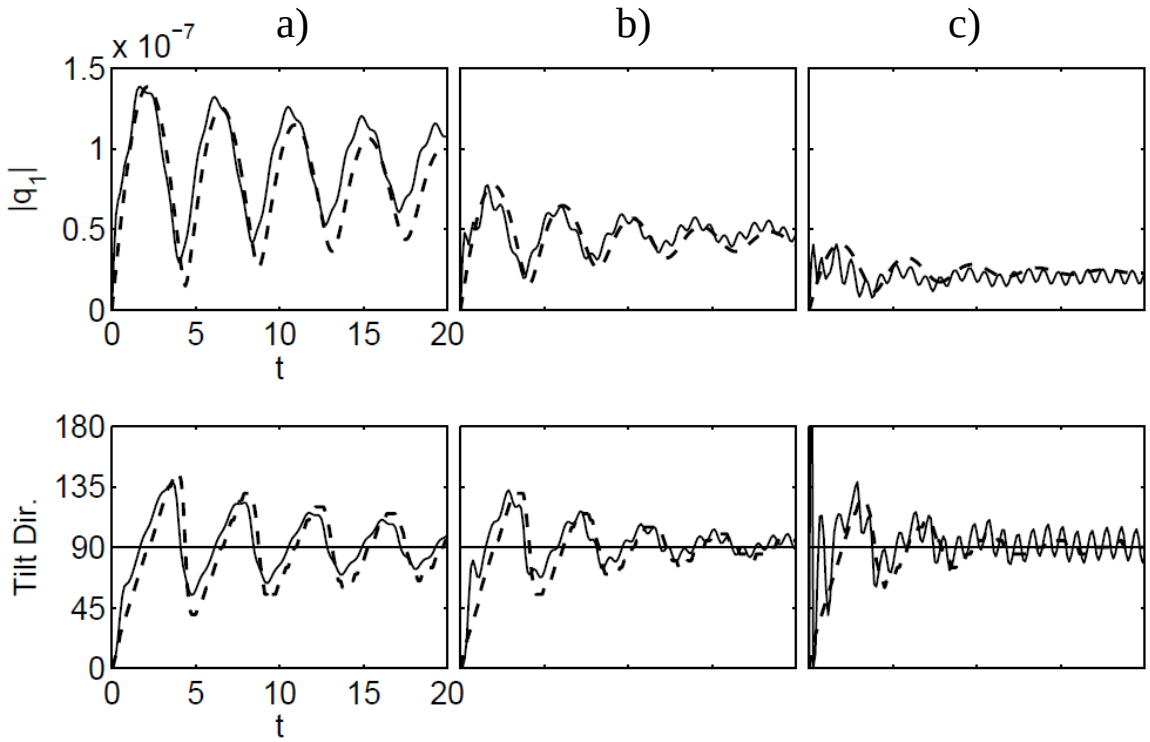

FIG. 9. Tilt amplitude and direction in the shear-forced (a) OBS1, (b) OBS2, (c) OBS3, (d) OBS4, and (e) OBS5 experiments. Tilt amplitude (top) is measured by the PV perturbation (s^{-3}) at the core radius r_c in OBS1-3 and at r = 40 km, radially outside the region of peak heating (cf. Fig. 7), in OBS4-5. Tilt direction is defined as the crest azimuth of the PV perturbation at $z = H$ (bottom). The solid lines show the simulated solution to the primitive equation model of Section 2, and the dashed lines show the heuristic model approximation to it using the decay rate and precession frequency from the respective free-alignment simulations. The heuristic model amplitude is scaled so as to match the initial peak-simulated value. Because the precession frequency and decay rate cannot be meaningfully estimated from the free-alignment solution in OBS5, values from OBS4 are used in the heuristic model solution in (e). 90º represents the left-of-shear direction, the equilibrium-tilt direction of the sheared vortex in all cases. Time is in units of circulation period at r_c.

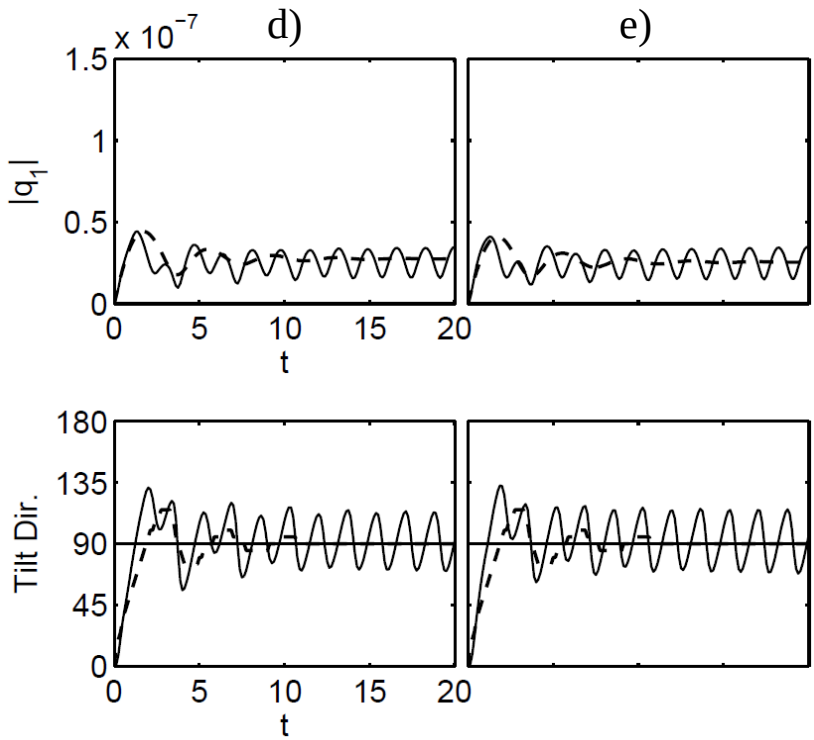
d)
e)
x 10^-7
1.5
1
0.5
0
|q1|
0
5
10
15
20
t
180
135
90
45
0
Tilt Dir.
0
5
10
15
20
t

FIG. 9. (cont'd)

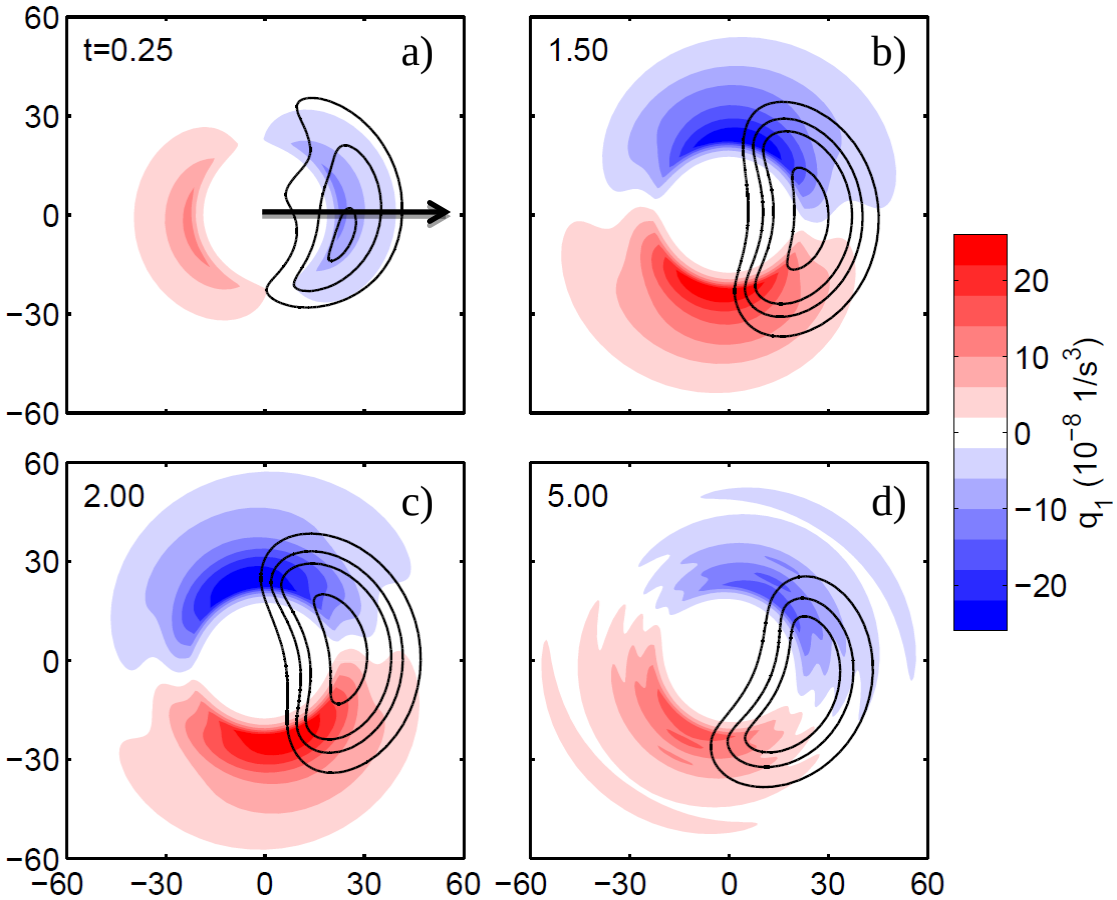

FIG. 10. Time evolution of core region PV perturbation (shaded, at z = 0) and positive vertical motion perturbation (at $z = H/2$) contoured at 0.25, 0.5, 0.75, and 1.5 ms^{-1} for the shear-forced OBS1 experiment. Vertical wind shear, indicated by the arrow in the top-left panel, is directed to the right. The fields are shown at (a) 0.25, (b) 1.5, (c) 2, and (d) 5 circulation periods. The early downshear-tilted vortex corresponds to a PV dipole with positive (negative) perturbation values upshear (downshear) at low levels. The horizontal scale is in km.

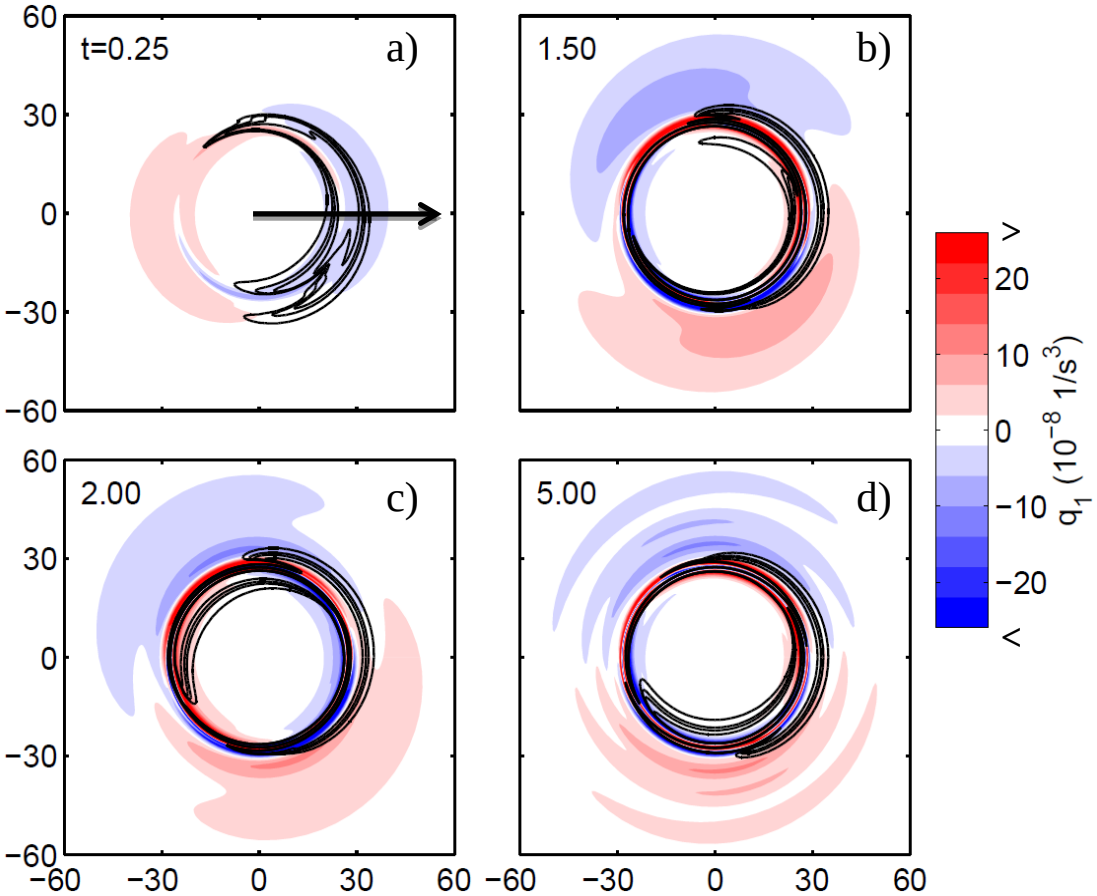

FIG. 11. As in Fig. 10, but for OBS5. Peak values of vertical motion and PV perturbation within the core exceed the contour ranges used in Fig. 10. To facilitate comparison of structure outside the core, the contour levels used in Fig. 10 are still employed here. See text for further discussion.

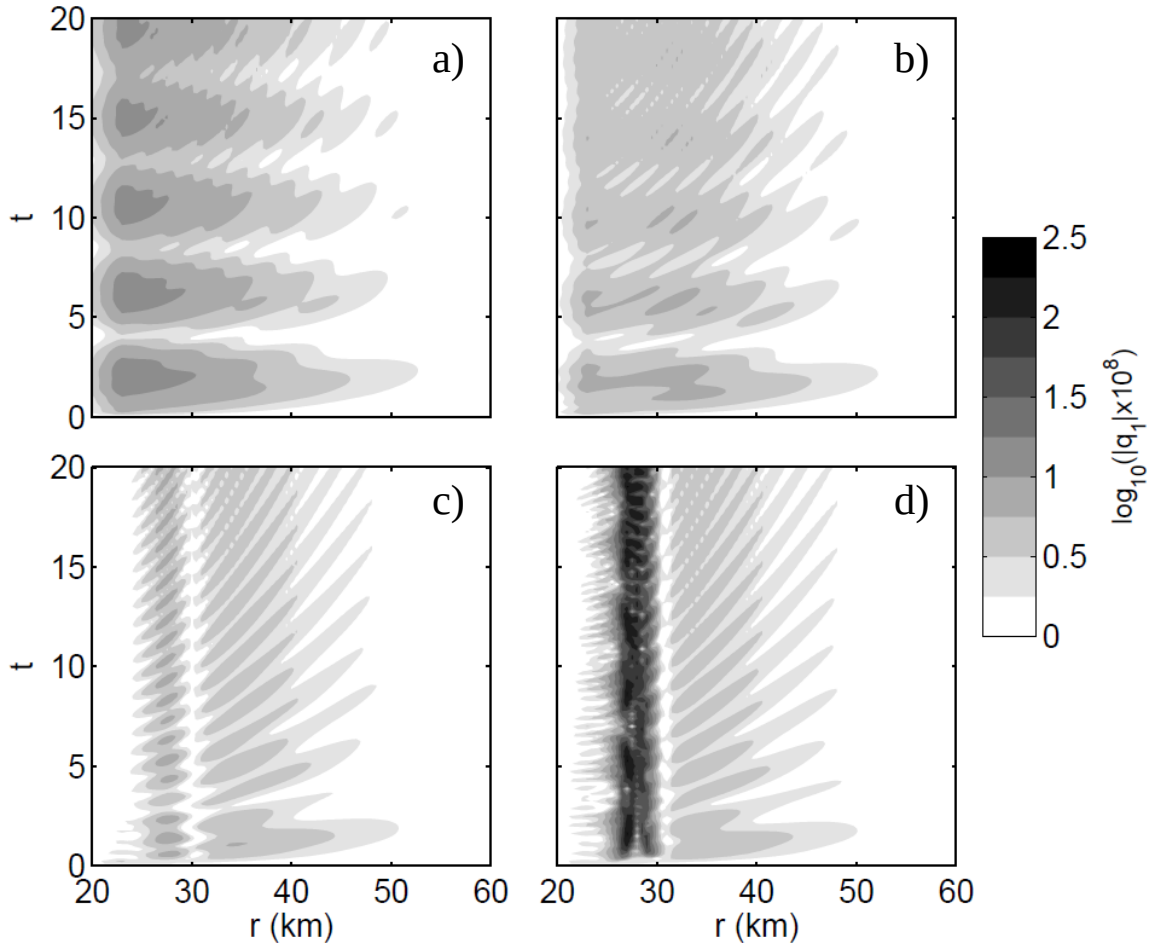

FIG. 12. Temporal evolution of the logarithmically-scaled PV amplitude within the core region in the shear-forced (a) OBS1, (b) OBS2, (c) OBS4, and (d) OBS5 experiments. Time is in units of circulation period at the core radius r_c.